CrossMark

Structural characterization and antibacterial activity of hydroxyapatite synthesized via sol-gel method using glutinous rice as a template

P. Phatai [1] · C. M. Futalan[2] · S. Kamonwannasit[3] · P. Khemthong[4]

Abstract

The present work aims to synthesize hydroxyapatite (HAp) via green template addition using glutinous rice (GR) in combination with sol-gel route under various calcination temperatures (500–900 °C). The physicochemical properties of GR-HAp were analyzed using X-ray diffraction, Fourier-transform infrared spectroscopy, scanning electron microscopy, transmission electron microscopy, and energy dispersive X-ray analysis. The utilization of GR as template in HAp synthesis resulted in the formation of GR-HAp particles that are less crystalline. Surface morphology revealed discrete, rod-shaped GR-HAp particles were formed at low calcination temperature (500–600 °C), while larger particles were formed as temperature was increased. Results confirmed that higher calcination temperature led to the transformation of HAp into various phases including β-Ca$_3$(PO$_4$)$_2$, CaO, and β-NaCa(PO$_4$). In addition, the formation of smaller, elongated GR-HAp particles with diameter of 75–180 nm and homogenous particle size distribution was attained at 900 °C. The antibacterial activity was evaluated via disc diffusion method against four Gram-positive bacteria including *B. cereus*, *B. subtilis*, *S. aureus*, and *S. epidermidis*, and two Gram-negative bacteria including *E. coli* and *P. aeruginosa*. The GR-HAp powder calcined at 900 °C showed strong antibacterial performance against all bacterial strains with inhibition zones ranging from 11.66–16.66 mm, which indicates its suitability to be utilized as a material in biomedical applications.

✉ P. Phatai
piaw.ph@udru.ac.th

[1] Department of Chemistry, Faculty of Science, Udon Thani Rajabhat University, Udon Thani 41000, Thailand

[2] National Research Center for Disaster-Free and Safe Ocean City, Busan 49315, Republic of Korea

[3] Department of Natural Product Technology, Faculty of Agricultural Technology, Burapha University, Sakaeo 27160, Thailand

[4] National Nanotechnology Center, National Science and Technology Development Agency, Pathumthani 12120, Thailand

SEM and HR-TEM images of GR-HAp900
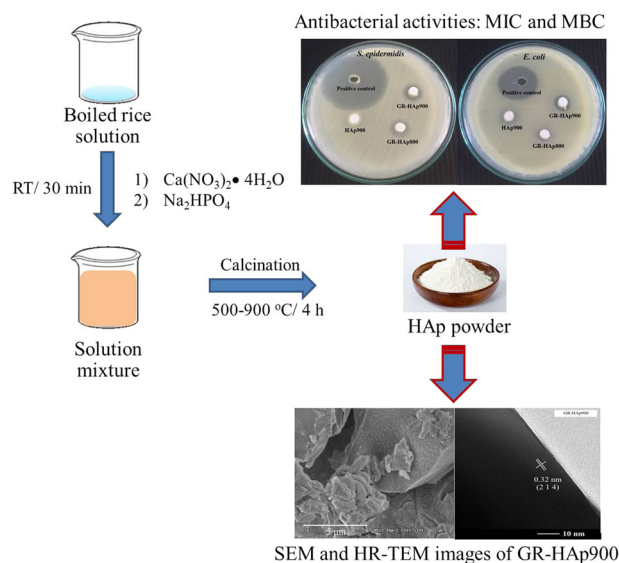
Highlights

- Use of GR as template resulted in formation of less crystalline particles with reduced aggregation.
- Higher calcination temperature led to formation of β-Ca$_3$ (PO$_4$)$_2$ and β-NaCa(PO$_4$) phases.
- GR-HAp calcined at 900 °C showed strongest antibacterial performance against all bacterial strains.

Keywords Hydroxyapatite · Sol-gel technique · Glutinous rice template · Calcination temperature · Antibacterial activity

1 Introduction

Hydroxyapatite (HAp: Ca$_{10}$(PO$_4$)$_6$(OH)$_2$) is a bioactive ceramic that is primarily composed of calcium and phosphate [1]. HAp occurs in two forms including the monoclinic and hexagonal phase with space group P2$_1$/b and P6$_3$/m, respectively [2]. The hexagonal structure of HAp is the main inorganic component found in the bone and teeth tissues of humans and animals [3]. HAp has a wide range of application in the field of medicine, water treatment, material science and biology, which is attributed to its excellent properties including high surface to volume ratio, non-toxicity, non-inflammatory, osteointegrity, stability under neutral and basic condition, non-immunogenicity, biocompatibility, bioactivity, low water solubility in acidic environment, and osteoconductivity and fracture toughness [4–9]. Over the years, HAp has been utilized in various industrial purposes such as heterogeneous catalyst [10], chemical and gas sensors [11, 12], chromatography for the separation and purification of nucleic acids and proteins [13], ion conductors [14], and adsorption treatment for the removal of Cd (II) and organic compounds (Congo red dye, malachite green dye, methyl blue dye, and methyl orange dye) from the aquatic environment [15–17]. Most importantly, HAp has been used extensively as a biomaterial in cell imaging and cancer treatment, repair of bone/tooth defects, implantation, and gene/drug delivery carrier and tissue engineering [18–22]. However, temperature, proper nutrition, and humidity of the human body in combination with the bioactivity of HAp would favor bacterial proliferation on implant surfaces causing severe physiological damage, wound infection, and implant failure [23–26]. Therefore, it is essential to assess the antibacterial activity and cytotoxicity of HAp and its modified forms in order to avoid supplementary medical procedures. Currently, HAp nanoparticles, with a grain size <100 nm in at least one direction, have attracted considerable interest especially in the field of implant–cell interaction in vivo [27] due to its enhanced biocompatibility, improved resorbability, high antibacterial and surface activity, and mechanical strength [28–30]. Moreover, the ultrafine structure of HAp results in the superior formation of bone tissue and osteointegration [30, 31].

Over the past decades, a number of conventional techniques have been employed in the fabrication of HAp such as microemulsion method, sol-gel, incipient wetness impregnation, wet chemical route, chemical precipitation, hydrothermal, solid-state reaction, mechanochemical method, and microwave heating [32–36]. The sol-gel reaction involves the mixing of alkoxides in an aqueous or organic phase to form a three-dimensional inorganic network. It is a cost-efficient method of mixing phosphorous and calcium monomers on a molecular level to attain chemical and structural uniformity under low temperature.

The sol-gel method has numerous advantages wherein the HAp particles produced are characterized by its nano-sized dimensions, stoichiometric structure, high purity, and improved surface area [30, 37, 38]. Recently, preparation of HAp via template addition in combination with any synthesis route offers effectivity in producing nanoparticles with homogenous morphology, narrow particle size distribution, and minimal particle aggregation [23]. The green template method often employs materials that are environmentally benign, readily available in large quantities, reactive under mild conditions, and derived from natural sources [39–42]. Previous works have successfully fabricated HAp nanoparticles using template materials such as alginate [43], carrageenan [5], chitosan [5, 44], or polysaccharides derived from various types of biomass such as aloe vera [40], banana [23], grape [23], tamarind [23], *Moringa oleifera* flower [45], and natural rubber latex [46]. Fang et al. [5] showed that the use of chitosan and carrageenan as templates promotes crystal growth modulation and heterogeneous nucleation of HAp crystals. The previous study of Gopi et al. [23] demonstrated formation of pure rod-shaped HAp nanoparticles using extracts from grape, banana, and tamarind, which also exhibited strong antibacterial activity.

Glutinous rice (*Oryza sativa* L.) (GR) is an essential ingredient in food and desserts served in festivals. GR is also considered as a staple food in the upland regions of Southeast Asia due to its low fat content and high content in protein, phenolic antioxidants (gallic acid, selenium, and kaempferol), amylose (linear glucose polymer), and amylopectin (branched polymer) [47–49]. In addition, GR is characterized by its solid appearance, soft consistency, and resistance to retrogradation [50]. The extensive application of GR as an industry resource is attributed to its high amylopectin content characterized by its distinct crystalline arrangement that is comprised of tandem linked clusters [51]. Based on extensive literature review, there are no reported studies on the antibacterial activity of HAp particles prepared with the hybrid technique of sol-gel procedure combined with the green template addition method using GR.

In the present work, HAp nanoparticles were fabricated via the sol-gel technique using GR as a green template. The effect of calcination temperature on the crystallinity, morphology, and particle size of GR-HAp was examined using X-ray diffraction (XRD), Fourier-transform infrared spectroscopy (FT-IR), scanning electron microscopy (SEM), transmission electron microscopy (TEM), and energy dispersive X-ray analysis (EDAX). Furthermore, the antibacterial activity against *Bacillus cereus*, *B. subtilis*, *Staphylococcus aureus*, *S. epidermis*, *Escherichia coli*, and *Pseudomonas aeruginosa* of HAp and GR-HAp particles was evaluated. The minimum inhibitory concentration (MIC) and minimum bactericidal concentration (MBC)

were determined via broth dilution method. The pathogenic bacteria selected in the study are the typical infections and diseases transmitted in hospitals.

2 Materials and methods

2.1 Materials and microorganisms

All chemical reagents were of analytical grade and utilized without further purification. Calcium nitrate tetrahydrate ($Ca(NO_3)_2 \cdot 4H_2O$, 99.9 wt.%), sodium hydroxide (NaOH, 96.0 wt.%) and di-sodium hydrogen phosphate (Na_2HPO_4, 99.0 wt.%) were acquired from QREC Chemical Co. Ltd. (Thailand). GR was obtained from Raitip, Thanya Farm Co. Ltd. (Thailand). The Gram-negative bacteria *E. coli* (TISTR 780) and *P. aeruginosa* (TISTR 781), and Gram-positive bacteria *S. aureus* (TISTR 1466), *S. epidermis* (TISTR 518), *B. subtilis* (TISTR 008), and *B. cereus* (TISTR 687) were acquired from the Thailand Institute of Scientific and Technological Research (TISTR), and were preserved using nutrient agar slants.

2.2 Synthesis of HAp

The synthesis of GR-HAp was carried out via sol-gel method using GR as a template. Firstly, the template solution was prepared by boiling dried GR seeds (4.0 g) in 100 mL deionized (DI) water at 70 °C for 3 h. Then, $Ca(NO_3)_2 \cdot 4H_2O$ (23.51 g) in 90 mL DI water and Na_2HPO_4 (8.48 g) in 60 mL DI water were dissolved to attain a final concentration of 1.11 and 1.00 M, respectively. In the template solution, $Ca(NO_3)_2 \cdot 4H_2O$ was slowly added under vigorous stirring at 25 °C for 0.5 h. After then, Na_2HPO_4 solution was added into the mixture in a drop-wise method under constant stirring for 0.5 h. After which, the pH of the mixture was adjusted to 10.0 using 1.0 M NaOH. The mixture was stirred continuously on a hotplate at 100 °C until dry. Finally, the dried samples were calcined in a muffle furnace (SNOL 30/1100 LSF21) for 4 h with a ramping rate of 3 °C/min. HAp particles using GR as template were calcined at various temperatures including 500 °C (GR-HAp500), 600 °C (GR-HAp600), 700 °C (GR-HAp700), 800 °C (GR-HAp800), and 900 °C (GR-HAp900), while samples synthesized without calcination are represented as HAp100 and GR-HAp100. For comparison, pure HAp was prepared without GR template and calcined at 900 °C (HAp900).

2.3 Characterization techniques

XRD patterns were recorded in the range of $2\theta = 20$–60° using CuKα radiation ($\lambda = 1.54184$ Å) at 40 kV and 35 mA
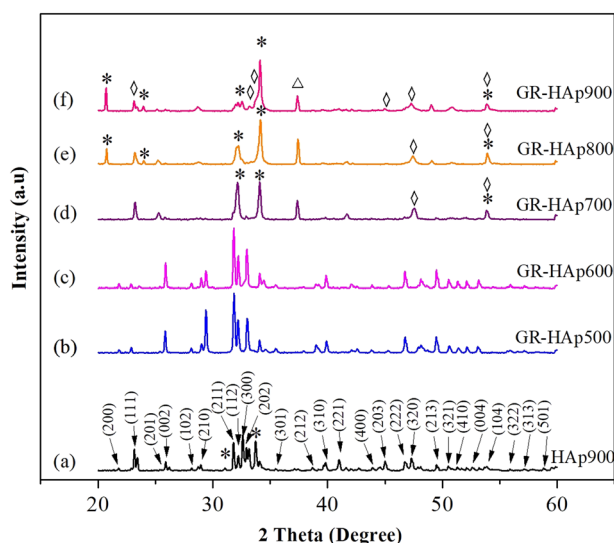
Fig. 1 XRD patterns of as-synthesized HAp samples under various calcination temperatures in air for 4 h with a ramp rate of 3 °C/min: (a) HAp900, (b) GR-HAp500, (c) GR-HAp600, (d) GR-HAp700, (e) GR-HAp800 and (f) GR-HAp900. [*β-TCP, β-NaCaPO$_4$, Δ CaO]

(D8 Advance Series 2 Bruker, Germany). The FT-IR analysis was carried out to identify the functional groups of HAp samples using the KBr disc method within the spectral range of 4000–500 cm^{-1} using a 4 cm^{-1} resolution (Spectrum two-Perkin Elmer, USA). The surface morphology was examined using SEM (Hitachi ModelS-3000N, Japan) with an accelerating voltage of 5 kV. TEM was utilized to analyze the particle size distribution and diameter of HAp samples operated at 200 kV (JEM-2100 Jeol, Japan). The elemental composition of Ca, P, Na, Mg, N, and O in HAp samples was determined using EDAX (S-3000N Hitachi, Japan).

2.4 Antibacterial activity

2.4.1 Disc diffusion method

The antibacterial activity of the GR-HAp was investigated by disc diffusion technique [52]. In a Mueller–Hinton broth (MHB), the bacterial strains were cultured at 37 °C for 18 h with a turbidity of 0.5 McFarland standard. Then, bacterial cultures (100 μL, 10^8 CFU/mL) were spread onto the Mueller–Hinton agar plate. The HAp samples (10 and 30 mg) dissolved in dimethyl sulfoxide (DMSO) was applied to sterilized filter paper discs (6 mm in diameter) and placed on the previously inoculated Mueller–Hinton agar. After which, the inoculated plates were incubated at 37 °C for 24 h. DMSO was used as a negative control, while tetracycline (30 μg/disc) was employed as a positive control. All disc diffusion tests were performed in triplicate and the diameters (mm) of the inhibition zone were measured after incubation.

2.4.2 Determination of minimum inhibition concentration and minimum bactericidal concentration

The determination of MIC and MBC against *S. epidermidis* and *P. aeruginosa* was conducted by a broth dilution method. MIC refers to the lowest concentration of the agents where no visible bacterial growth is observed after a 24 h incubation at 37 °C, while MBC is defined as the lowest concentration of agent where there is no occurrence of subculture growth [53]. Based on the methodology of Kamonwannasit et al. [53], the MIC against bacteria (10^7 CFU/mL) was performed with various concentrations of GR-HAp900 in MHB where incubation of the inoculated tubes was carried out at 37 °C for 24 h. MBC was determined where 100 μL from each tube with no visible bacterial growth was subcultured onto fresh Mueller–Hinton agar plate and incubated at 37 °C for 24 h. All experimental runs were performed in triplicate.

3 Results and discussion

3.1 Crystal phase analysis by XRD

The XRD spectra of HAp100 and GR-HAp100 samples are illustrated in Fig. S1, while the XRD patterns of synthesized HAp and GR-HAp samples under various calcination temperatures are shown in Fig. 1. Based on Fig. S1, the crystalline structure of GR-HAp100 is illustrated by broader and dispersed peaks within the 2θ range from 31.0° to 34.0°. The low crystallinity of GR-HAp100 is attributed to the incomplete reaction between Ca(NO$_3$)$_2$•4H$_2$O and Na$_2$HPO$_4$ as well as the presence of organic compounds in GR that were not removed completely [54]. The XRD spectrum of HAp100 exhibited triclinic monetite (CaHPO$_4$) crystal with space group *P-1* and corresponding peaks 2θ at 20.4°, 26.62°, 29.6°, 30.44°, 36.29°, and 41.2° (JCPDS card no. 77-0128). In addition, the pure HAp phase was not detected in the uncalcined samples.

In Fig. 1, the XRD spectrum of HAp900 exhibited stoichiometric hexagonal HAp crystal with space group $P_{63}/_m$ with corresponding peaks of 2θ at 25.8° (0 0 2), 31.8° (2 1 1), 32.9° (1 1 2), 34.1° (2 0 2), 39.8° (3 1 0), 46.7° (2 2 2), and 49.5° (2 1 3) (JCPDS card no. 09-0432). The two peaks located at 2θ = 31.0° (0 2 10) and 34.4° (2 2 0) belong to β-Ca$_3$(PO$_4$)$_2$ (β-TCP) with rhombohedral structure in space group *R-3c* (JCPDS card no. 09-0169). A high Ca/P ratio (1.88) and high calcination temperature of 900 °C resulted in the decrease in HAp purity and led to the formation of β-TCP [55]. Moreover, the previous study of Esfahani et al. [56] found that a calcination temperature of 1000 °C can cause Zn-doped HAp to decompose into β-TCP and β–Zn$_3$(PO$_4$)$_2$. The spectra of GR-HAp synthesized

at low calcination temperature (500–600 °C) have more similar peaks with standard HAp over that of HAp900. In addition, the peaks of GR-HAp500 and GR-HAp600 are sharper and more narrow, which implies that HAp powders have higher crystallinity. Further increasing the calcination temperature from 700 to 900 °C resulted in the appearance of several phases including β-TCP as the main phase while β-NaCaPO$_4$ (JCPDS card no. 76-1456) and CaO (JCPDS card no. 48-1467) were detected as minor phases. The small peak detected at 37.5° was attributed to the (2 0 0) plane of CaO, which could be due to decomposition of HAp caused by chemical impurities or elevated temperature [54, 57, 58]. When the calcination temperature is set at 700 °C and above, the concentration of carbonates in pure HAp was observed to decrease [59]. In the phase transformation from HAp to β-TCP, it has been previously reported that the reaction temperature also plays an essential role. Using calcium deficient HAp, the formation of β-TCP occurs at a calcination temperature range of 800–1340 °C that could be due to the nano-sized HAp particles, which are sensitive to heat treatment [54, 55, 60]. Meanwhile, the presence of β-NaCaPO$_4$ was due to the interstitial incorporation of Na$^+$ into the HAp lattice [61].

3.2 FT-IR analysis

Figure 2 illustrates the FT-IR spectra of uncalcined HAp, pure HAp, and HAp synthesized using GR template. The peaks of uncalcined samples (Fig. 2a, b) are less distinct and wider when compared to calcined HAp samples. The following bands indicate the presence of HAp: 1048 cm^{-1} is due to the υ_3 modes of phosphate groups, 3639 cm^{-1} refers to the stretching vibration of hydroxyl groups, 1641 cm^{-1} due to bending mode of lattice water, and 1420 cm^{-1} for the carbonate peaks [6, 23]. In pure HAp (Fig. 2c), the following sharp bands at 955 cm^{-1} and within the range of 1048–1082 cm^{-1} correspond to the symmetric $\nu1$ stretching mode (P–O bond) and $\nu2$ bending mode (O–P–O bond) of tetragonal PO$_4^{3-}$. The bands at 571 and 618 cm^{-1} indicate the asymmetric $\nu3$ stretching (P–O bond) and $\nu4$ bending (O–P–O bond) vibration modes in PO$_4^{3-}$ [62]. The sharp bands at 3639 and 640 cm^{-1} refer to –OH stretching and bending vibrations, respectively. Moreover, these peaks are typical characteristics of stoichiometric HAp that are not involved in hydrogen bonding within the crystal lattice [6, 63]. The broad peaks at 3476 and 1641 cm^{-1} occurred in GR-HAp calcined at low temperatures (500–600 °C), which indicate the stretching and bending mode of physisorbed water molecules [23]. Furthermore, the bands within range of 1400–1556 cm^{-1} and a sharp peak at 873 cm^{-1} represent C = O and C–O stretching vibrations of carbonate $\left(CO_3^{2-}\right)$, which is due to the dissolution of atmospheric CO$_2$ into the aqueous solution during synthesis [64, 65]. After which,
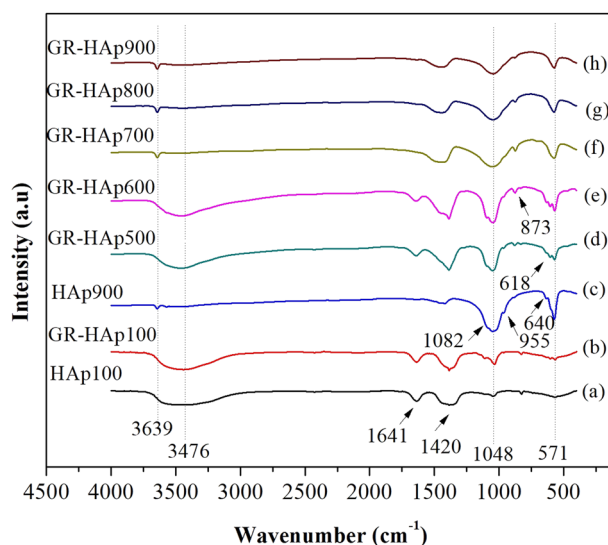

Fig. 2 FT-IR spectra of as-synthesized HAp samples under various calcination temperatures in air for 4 h with a ramp rate of 3 °C/min: (a) HAp100, (b) GR-HAp100, (c) HAp900, (d) GR-HAp500, (e) GR-HAp600, (f) GR-HAp700, (g) GR-HAp800 and (h) GR-HAp900

aqueous CO$_3^{2-}$ is integrated as part of the amorphous complex and becomes part of the low crystalline HAp [56]. In the GR-HAp samples, the low quantity of carbonate present implies that carbonate substituted HAp was not produced, as validated by the XRD results [66]. The peak at 873 cm^{-1} refers to the marginal substitution of the phosphate group with the carbonate group, which implies that the sample is classified as a B-type HAp [67, 68].

3.3 SEM, TEM, and EDX

The surface morphology of GR-HAp powders calcined at 500–900 °C was characterized using SEM-EDAX and TEM. In Fig. 3a, the SEM micrograph of HAp900 shows irregular, non-homogenous morphology of agglomerated pure HAp with a non-uniform particle size distribution. Calcination of GR-HAp at low temperature (500–600 °C) resulted in the formation of discrete rod-shaped HAp particles (Fig. 3b, c), which could be due to the formation of elongated crystallites along the crystallographic c-axis direction of HAp samples [69]. However, Fig. 3b exhibits spherical particles with size range of 2–3 μm that have accumulated onto the surface of larger, elongated HAp particles. Meanwhile, Fig. 3c displays smaller HAp particles with an average length and diameter of ~1.5 and 0.2 μm, respectively. Increasing the calcination temperature to 700 °C or greater would lead to the formation of large, indistinguishable particles where agglomeration of HAp is evident.

Figure 4a, b illustrates the TEM micrographs of pure HAp and GR-HAp calcined at 900 °C. Based on Fig. 4a, the morphology of HAp900 exhibits large, oval-shaped

Fig. 3 SEM images of as-synthesized HAp samples under various calcination temperatures in air for 4 h with a ramp rate of 3 °C/min: (a) HAp900, (b) GR-HAp500, (c) GR-HAp600, (d) GR-HAp700, (e) GR-HAp800and (f) GR-HAp900
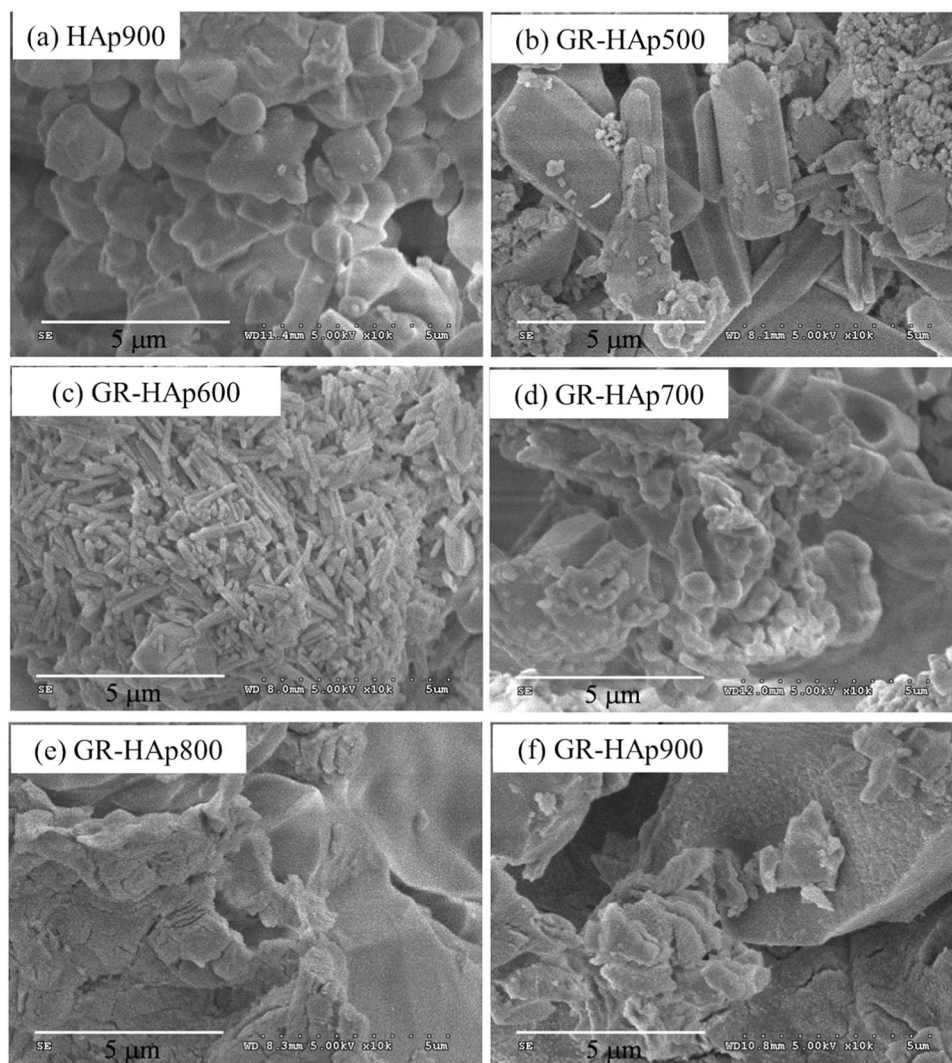
particles with diameter ranging from 430 to 570 nm. In Fig. 4b, the agglomeration of small, elongated and rod-shaped particles with diameter of ~75–180 nm was observed. Moreover, the GR-HAp900 particles are characterized by its homogenous particle size distribution that can be attributed to the presence of polysaccharides derived from GR solution [40]. The crystalline structure of HAp900 (Fig. 4c) and GR-HAp900 (Fig. 4d) was further confirmed by high-resolution TEM. Expected lattice fringes are displayed by HAp900 and GR-HAp900 particles with an interplanar spacing of 0.34 and 0.32 nm, respectively. This corresponds to the (0 0 2) plane of HAp and (2 1 4) plane of β-TCP. Overall, the observations are in good agreement with the XRD patterns.

The chemical composition of HAp900, GR-HAp500, and GR-HAp900 is depicted in Fig. 5. Based on the EDAX patterns, the principal constituents of HAp900, GR-HAp500, and GR-HAp900 were determined to be Ca, P,

Na, and O. The presence of Na in HAp samples is attributed to the use of Na_2HPO_4 as a precursor and NaOH for pH adjustment, which were employed in the preparation of the biomaterial. For GR-HAp900, traces of Mg were detected that could be attributed to the GR solution. The presence of Na and Mg in as-synthesized GR-HAp900 is advantageous due to its considerable antibacterial properties against *E. coli* and *S. aureus* [70, 71]. The trace amount of N in GR-HAp500 and GR-HAp600 was detected, which can be attributed to proteins consisted in GR that were not removed completely at 500 and 600 °C. On the other hand, the presence of C can be attributed to the carbon tape mounted onto SEM stub during analysis. Based on Table 1, the Ca/P molar ratio of the samples is found within the range of 1.88–3.94. When compared with the stoichiometric HAp ratio (1.67), the higher values of Ca/P ratio of the synthesized HAp samples could be attributed to the substitution of PO_4^{3-} by CO_3^{2-} [72, 73].
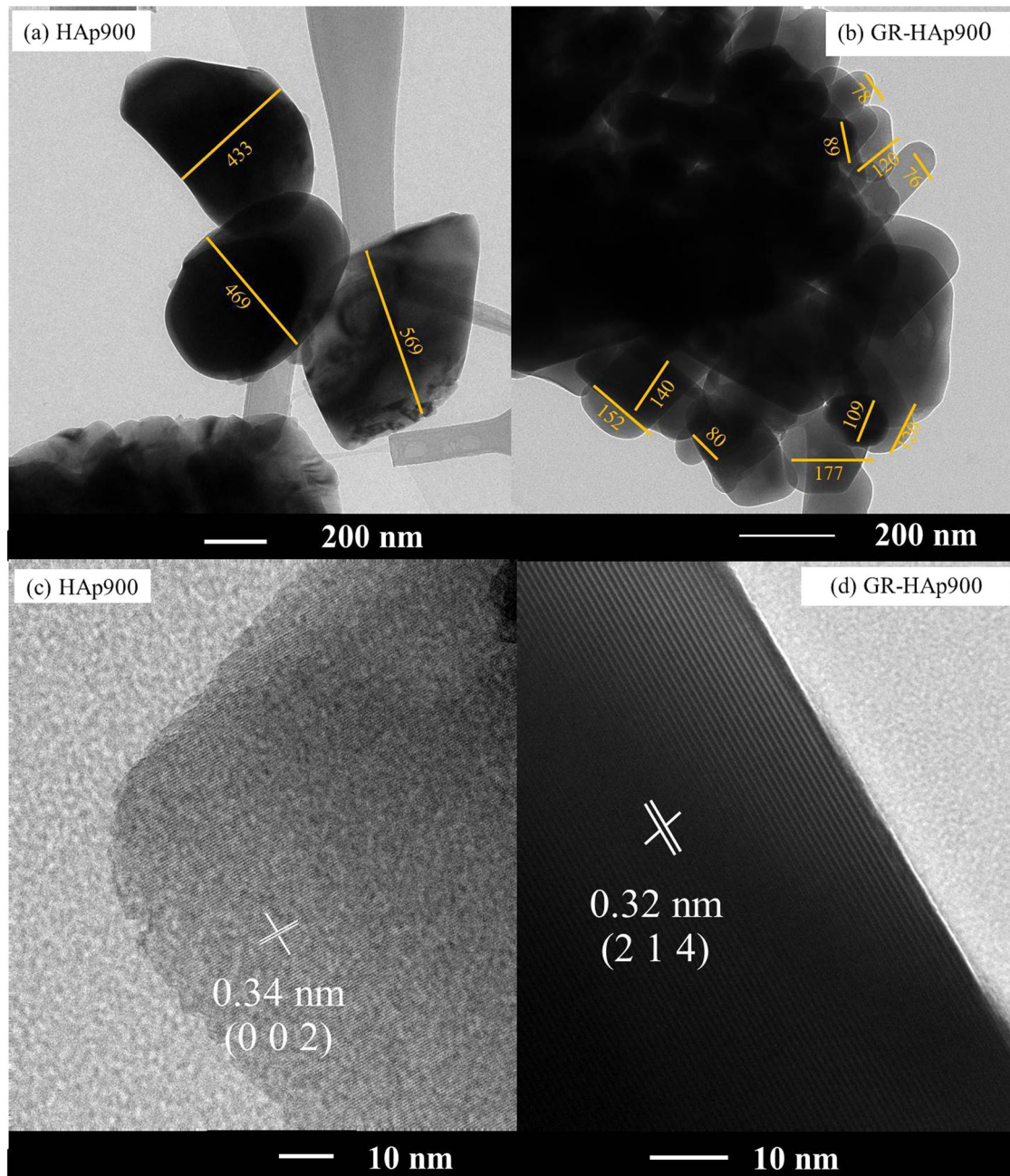
Fig. 4 TEM and HR-TEM micrographs of HAp synthesized (**a**, **c**) without GR template and calcined at 900 °C and (**b**, **d**) with GR template and calcined at 900 °C

3.4 Antibacterial activities

The antibacterial activity of HAp-900 and GR-HAp samples under various concentrations (10 and 30 mg) was evaluated against six strains of bacteria. As shown in Table 2 and Fig. 6, the positive control tetracycline was effective against all bacterial strains at 30 µg where inhibition zones range from 21 to 40 mm. Of the as-synthesized HAp powders, HAp900, GR-HAp500, GR-HAp600, and GR-HAp700

exhibited no inhibition of bacterial growth against all strains. Only GR-HAp700 at a dose of 30 mg demonstrated inhibited growth against *P. aeruginosa* with an inhibition zone of 10.33 mm. In GR-HAp800, all strains were not inhibited at 10 mg. Further increasing the dose to 30 mg, the presence of inhibition zone ranging from 7 to 13 mm in all bacterial strains was observed, where the highest inhibition zone of 13 mm was displayed by *B. cereus*. The GR-HAp900 samples at 10 mg exhibited antibacterial activities
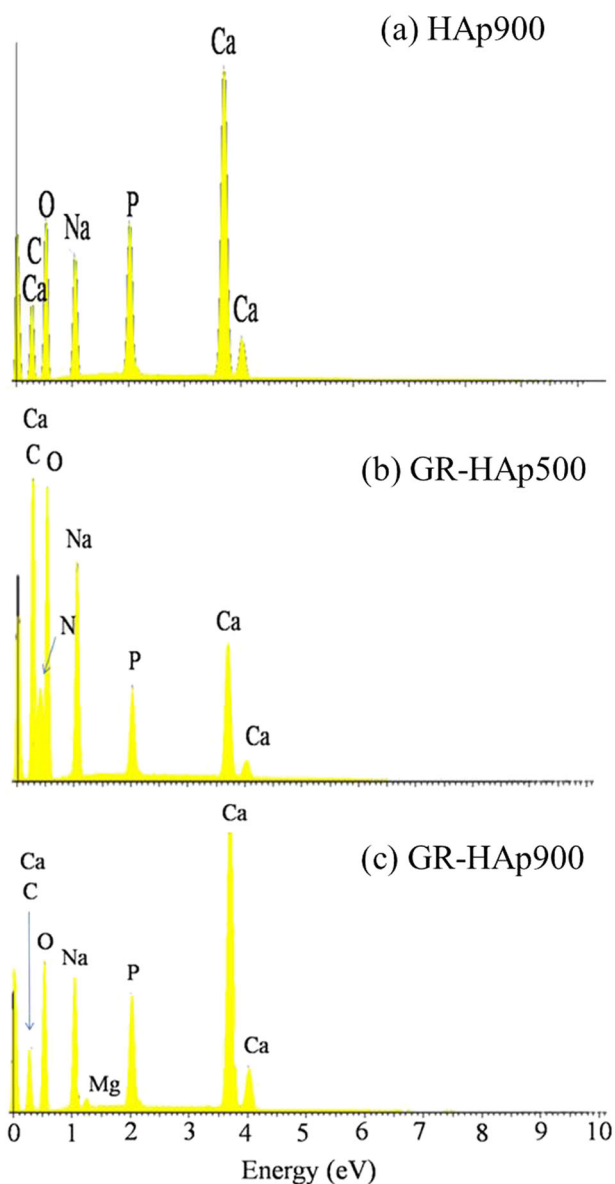
Fig. 5 EDX spectra of (a) HAp900, (b) GR-HAp500, and (c) GR-HAp900

against *S. epidermidis* and *P. aeruginosa* with inhibition zone of 8.33 and 8.66 mm, respectively. Meanwhile, all bacterial strains were inhibited at 30 mg of GR-HAp900, where the greatest diameter of inhibition zone (15–16.66 mm) was observed for *S. aureus* and *S. epidermis*.

The antibacterial activity can be attributed to the presence of minerals such as Na^+ and Ca^{2+} contained in the as-synthesized HAp that may have originated from GR solution and Na_2HPO_4, which was utilized as precursor in HAp preparation. However, samples including HAp900, GR-HAp500, GR-HAp600, and GR-HAp700 did not exhibit any antibacterial activities. Even though all HAp samples contain trace amount of Na^+ and Ca^{2+}, the difference in crystal structure and secondary phases present under different calcination temperatures has greater effect on the antibacterial activity. Samples such as HAp900, GR-HAp500, and GR-HAp600 displayed almost pure phase of HAp, while GR-HAp calcined at higher temperatures demonstrated mixed phases of β-TCP, CaO, and β-NaCaPO4. The antibacterial property of GR-HAp900 is found to be the highest among the as-synthesized HAp powders against all bacterial strains. This is attributed to the GR-HAp900 having the highest content for Ca^{2+} (22.42%) and Na^+ (9.46%) and presence of β-TCP where there is better solubility and bioresorbability of Mg^{2+} and Na^+ that would result in improved antibacterial activity [23, 74]. The high solubility is due to the small value of the negative logarithm of the solubility product of β-TCP (pK_{sp} = 28.90) when compared to that of HAp (pK_{sp} = 116.80) [75]. Several studies have shown that longer immersion time results in higher amount of Ca^{2+} released from β-TCP. The study of Li et al. [76] showed that release of Ca^{2+} from β-TCP in 1.5, 3, and 27 months is 4.44, 4.61, and 5.16 mM, while Jamil et al. [75] revealed that 1 and 3 h immersion resulted in the release of 174 and 211 mg/L Ca^{2+}. In addition, Xie and Yang [77] has shown that higher antibacterial activity against *S. aureus* was attained at higher dosage of Ca^{2+}.

Samples	wt. %							Ca/P
	Ca (K)[a]	P (K)[a]	Na (K)[a]	Mg (K)[a]	N (K)[a]	O (K)[a]	C (K)[a]	
HAp900	17.41	9.26	4.42	—	—	40.69	28.22	1.88
GR-HAp500	4.76	2.04	7.07	—	7.07	41.39	32.95	2.33
GR-HAp600	4.42	2.02	6.13	—	11.44	40.52	35.47	2.18
GR-HAp700	20.29	7.04	7.85	—	—	44.92	19.90	2.88
GR-HAp800	20.42	6.45	8.39	—	—	45.14	19.60	3.17
GR-HAp900	22.42	5.69	9.46	0.11	—	45.51	16.81	3.94

Table 1 Weight percentages of Ca, P, Na, Mg, N, O, and C in HAp and GR-HAp samples derived from the EDX measurements

[a]The shells to which electron transition are shown for each element

Table 2 Diameter of inhibition zones of as-synthesized HAp samples against six different types of bacterial strains

Types of bacteria	Inhibition diameter (mm)		Tetracycline (30 µg)
	10 mg	30 mg	
HAp900			
Bacillus cereus	ND	ND	—
Bacillus subtilis	ND	ND	—
Staphylococcus aureus	ND	ND	—
Staphylococcus epidermidis	ND	ND	—
Escherichia coli	ND	ND	—
Pseudomonas aeruginosa	ND	ND	—
GR-HAp500			
Bacillus cereus	ND	ND	—
Bacillus subtilis	ND	ND	—
Staphylococcus aureus	ND	ND	—
Staphylococcus epidermidis	ND	ND	—
Escherichia coli	ND	ND	—
Pseudomonas aeruginosa	ND	ND	—
GR-HAp600			
Bacillus cereus	ND	ND	—
Bacillus subtilis	ND	ND	—
Staphylococcus aureus	ND	ND	—
Staphylococcus epidermidis	ND	ND	—
Escherichia coli	ND	ND	—
Pseudomonas aeruginosa	ND	ND	—
GR-HAp700			
Bacillus cereus	ND	ND	—
Bacillus subtilis	ND	ND	—
Staphylococcus aureus	ND	ND	—
Staphylococcus epidermidis	ND	ND	—
Escherichia coli	ND	ND	—
Pseudomonas aeruginosa	ND	10.33 ± 0.57	—
GR-HAp800			
Bacillus cereus	ND	13.00 ± 0.00	—
Bacillus subtilis	ND	7.66 ± 0.58	—
Staphylococcus aureus	ND	11.00 ± 1.00	—
Staphylococcus epidermidis	ND	12.00 ± 1.00	—
Escherichia coli	ND	10.33 ± 0.58	—

Table 2 (continued)

Types of bacteria	Inhibition diameter (mm)		Tetracycline (30 µg)
	10 mg	30 mg	
Pseudomonas aeruginosa	ND	10.66 ± 0.58	—
GR-HAp900			
Bacillus cereus	ND	12.33 ± 0.57	—
Bacillus subtilis	ND	12.00 ± 0.00	—
Staphylococcus aureus	ND	15.00 ± 0.00	—
Staphylococcus epidermidis	8.33 ± 1.52	16.66 ± 0.57	—
Escherichia coli	ND	12.66 ± 0.57	—
Pseudomonas aeruginosa	8.66 ± 0.58	11.66 ± 2.88	—
Tetracycline			
Bacillus cereus	—	—	21.00 ± 0.00
Bacillus subtilis	—	—	22.00 ± 2.82
Staphylococcus aureus	—	—	33.00 ± 0.00
Staphylococcus epidermidis	—	—	40.00 ± 0.00
Escherichia coli	—	—	27.50 ± 0.70
Pseudomonas aeruginosa	—	—	21.50 ± 0.70

ND no detection

Table 3 illustrates the MIC and MBC values of GR-HAp900 against *S. epidermidis* and *P. aeruginosa*. The MIC values of 4 and 6 mg/mL were attained for *S. epidermidis* and *P. aeruginosa*, respectively where the greatest activity was demonstrated against Gram-positive bacteria *S. epidermidis* with lower MIC value obtained. On the other hand, the bactericidal activity was determined with MBC values of >12 mg/mL for both strains. Based on the MIC values, *S. epidermidis* is more sensitive to GR-HAp900 when compared to *P. aeruginosa*. Results could be due to the structural differences in the outer membrane of varying bacterial strains. The outer membrane of the Gram-negative bacteria is characterized by a cell wall comprised of a thick layer of structural lipopolysaccharides in the periplasmic space that is located between the inner and outer lipid membranes. Hence, the cell wall's complexity would render the microbe impermeable to lipophilic solutes with an improved resistance to chemical agents [78]. Moreover, the presence of numerous efflux pumps in a Gram-negative bacteria prevents the accumulation of antibacterial agents within the cell membrane [74]. On the other hand, Gram-

Fig. 6 Photographs of the antibacterial activity of HAp900, GR-HAp800, and GR-HAp900 against (**a**) Gram-positive bacteria *S. epidermidis* and (**b**) Gram-negative bacteria *E. coli* at a dose of 30 mg/mL
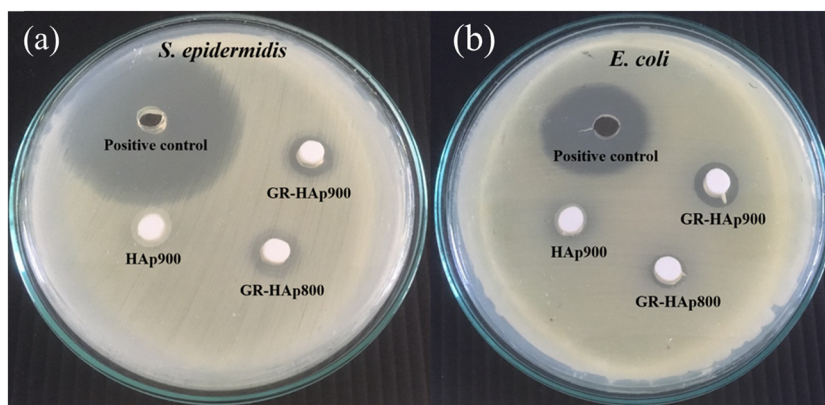

Table 3 MIC and MBC of GR-HAp900 against *S. epidermis* and *P. aeruginosa*

Microorganisms	Concentration (mg/mL)	
	MIC	MBC
S. epidermidis	4	>12
P. aeruginosa	6	>12

positive bacteria does not possess this type of outer membrane but is characterized by its relatively simple cell wall comprised of lipoteichoic acids and a single layer of peptidoglycan [1, 78, 79].

4 Conclusions

GR-HAp particles were successfully synthesized via sol-gel method with GR as a green template and calcined under varying temperature. Results of the XRD analysis confirmed formation of pure crystalline HAp at low calcination temperature (500–600 °C). The HAp was transformed to various crystal phases including β-TCP, CaO, and β-NaCaPO$_4$ at higher temperature range (700–900 °C). SEM and TEM images revealed that addition of GR template resulted in the formation of HAp particles that are discrete and homogenous in nature. The disc diffusion method was employed to investigate the antibacterial activity against six strains of bacteria. Results illustrated that GR-HAp900 exhibited excellent antibacterial activity against Gram-positive and Gram-negative bacteria. Hence, eco-friendly and non-toxic GR-HAp particles can be used as a potential material in biomedical applications.

Compliance with ethical standards

Conflict of interest The authors declare that they have no conflict of interest.

Publisher's note: Springer Nature remains neutral with regard to jurisdictional claims in published maps and institutional affiliations.

References

1. Moldovan M, Prodan D, Sarosi C, Carpa R, Socaci C, Rosu MC, Oruneanu S (2018) Synthesis, morpho-structural properties and antibacterial effect of silicate-based composites containing graphene oxide/hydroxyapatite. Mater Chem Phys 217:48–53
2. Chiatti F, Corno M, Ugliengo P (2012) Stability of the dipolar (001) surface of hydroxyapatite. J Phys Chem C 116:6108–6114
3. Hench LL (1991) Bioceramics: from concept to clinic. J Am Ceram Soc 74:1487–1510
4. Piccirillo C, Castro PML (2017) Calcium hydroxyapatite-based photocatalysts for environment remediation: characteristics, performances and future perspectives. J Environ Manag 193:79–91
5. Fang W, Zhang H, Yin J, Yang B, Zhang Y, Li J, Yao F (2016) Hydroxyapatite crystal formation in the presence of polysaccharide. Cryst Growth Des 16:1247–1255
6. Gopi D, Indira J, Kavitha L, Sekar M, Mudali UK (2012) Synthesis of hydroxyapatite nanoparticles by a novel ultrasonic assisted with mixed hollow sphere template method. Spectrochim Acta Part A 93:131–134
7. Rajzer I, Kwiatkowski R, Piekarczyk W, Binias W, Janicki J (2012) Carbon nanofibers produced from electrospun PAN/HAp precursors as scaffolds for bone tissue engineering. Mater Sci Eng C 32:2562–2569
8. Weiner S, Wagner HD (1998) The material bone: structure-mechanical function relations. Annu Rev Mater Sci 28:271–298
9. Chandra VS, Baskar G, Suganthi RV, Elayaraja K, Joshy MI, Beaula WS, Mythili R, Venkatraman G, Kalkura SN (2012) Blood compatibility of iron-doped nanosize hydroxyapatite and its drug release. ACS Appl Mater Interfaces 4:1200–1210
10. Fihri A, Len C, Varma RS, Solhy A (2017) Hydroxyapatite: a review of synthesis, structure and applications in heterogeneous catalysis. Coord Chem Rev 347:48–76
11. Xie Y, Perera TSH, Li F, Han Y, Yin M (2015) Quantitative detection method of hydroxyapatite nanoparticles based on Eu^{3+} fluorescent labeling in vitro and in vivo. ACS Appl Mater Interfaces 7:23819–23823

12. Mahabole MP, Aiyer RC, Ramakrishna CV, Sreedhar B, Khairmar RS (2005) Synthesis, characterization and gas sensing property of hydroxyapatite ceramic. Bull Mater Sci 28:535–545

13. Kandori K, Oketani M, Wakamur M (2013) Effects of Ti(IV) substitution on protein adsorption behaviors of calcium hydroxyapatite particles. Colloids Surf B 101:68–73

14. Bouhaouss A, Bensaoud A, Laghzizil A, Ferhat M (2001) Effect of chemical treatments on the ionic conductivity of carbonate apatite. Int J Inorg Mater 3:437–441

15. Guan Y, Cao W, Guan H, Lei X, Wang X, Tu Y, Marchetti A, Kong X (2018) A novel polyalcohol-coated hydroxyapatite for the fast adsorption of organic dyes. Colloids Surf A 548:85–91

16. Zhu XH, Li J, Luo JH, Jin Y, Zheng D (2017) Removal of cadmium (II) from aqueous solution by a new adsorbent of fluorhydroxyapatite composites. J Taiwan Inst Chem Eng 70:200–208

17. Hosseinzadeh H, Ramin S (2018) Fabrication of starch-graft-poly (acrylamide)/graphene oxide/hydroxyapatite nanocomposite hydrogel adsorbent for removal of malachite green dye from aqueous solution. Int J Biol Macromol 106:101–115

18. Kutikov AB, Skelly JD, Ayers DC, Song J (2015) Templated repair of long bone defects in rats with bioactive spiral-wrapped electrospun amphiphilic polymer/hydroxyapatite scaffolds. ACS Appl Mater Interfaces 7:4890–4901

19. Epple M, Ganesan K, Heumann R, Klesing J, Kovtun A, Neumann S, Sokolova V (2010) Application of calcium phosphate nanoparticles in biomedicine. J Mater Chem 20:18–23

20. Zhang X, Hui J, Yang B, Yang Y, Fan D, Liu M, Tao L, Wei Y (2013) PEGylation of fluoridated hydroxyapatite (FAp):Ln^{3+} nanorods for cell imaging. Polym Chem 4:4120–4125

21. Hou CH, Hou SM, Hsueh YS, Lin J, Wu HC, Lin FH (2009) The in vivo performance of biomagnetic hydroxyapatite nanoparticles in cancer hyperthermia therapy. Biomaterials 30:3956–3960

22. Li J, Yin Y, Yao F, Zhang L, Yao K (2008) Effect of nano- and micro-hydroxyapatite/chitosan-gelatin network film on human gastric cancer cells. Mater Lett 62:3220–3223

23. Gopi D, Bhuvaneshwari N, Indira J, Kanimozhi K, Kavitha L (2013) A novel green template assisted synthesis of hydroxyapatite nanorods and their spectral characterization. Spectrochim Acta Part A 107:196–202

24. Crémet L, Corvec S, Bémer P, Bret L, Lebrun C, Lesimple B, Miegeville AF, Reynaud A, Lepelletier D, Caroff N (2012) Orthopaedic-implant infections by *Escherichia coli*: molecular and phenotypic analysis of the causative strains. J Infect 64:169–175

25. Khan MS, ur Rehman S, Ali MA, Sultan B, Sultan S (2008) Infection in orthopedic implant surgery, its risk factors and outcome. J Ayub Med Coll Abbottabad 20:23–25

26. Salwiczek M, Qu Y, Gardiner J, Strugnell RA, Lithgow T, McLean KM, Thissen H (2014) Emerging rules for effective antimicrobial coatings. Trends Biotechnol 32:82–90

27. Dorozhkin SV, Epple M (2002) Biological and medical significance of calcium phosphates. Angew Chem Int Ed Engl 41:3130–3146

28. Zhou H, Lee J (2011) Nanoscale hydroxyapatite particles for bone tissue engineering. Acta Biomater 7:2769–2781

29. Vallet-Regí M, González-Calbet JM (2004) Calcium phosphates as substitution of bone tissues. Prog Solid State Chem 32:1–31

30. Dong Z, Li Y, Zou Q (2009) Degradation and biocompatibility of porous nano-hydroxyapatite/polyurethane composite scaffold for bone tissue engineering. Appl Surf Sci 255:6087–6091

31. Sadat-Shojai M, Khorasani MT, Dinpanah-Khoshdargi E, Jamshidi A (2013) Synthesis methods for nanosized hydroxyapatite with diverse structures. Acta Biomater 9:7591–7621

32. Liu Y, Hou D, Wang G (2004) A simple wet chemical synthesis and characterization of hydroxyapatite nanorods. Mater Chem Phys 86:69–73

33. Ashuri M, Moztarzadeh F, Nezafati N, Hamedani AA, Tahriri M (2012) Development of a composite based on hydroxyapatite and magnesium and zinc-coating sol-gel-derived bioactive glass for bone substitute applications. Mater Sci Eng C 32:2330–2339

34. Fahami A, Nasiri-Tabrizi B, Ebrahimi-Kahrizsangi R (2012) Synthesis of calcium phosphate-based composite nanopowders by mechanochemical process and subsequent thermal treatment. Ceram Inter 38:6729–6738

35. Farzadi A, Solati-Hashjin M, Bakhshi F, Aminian A (2011) Synthesis and characterization of hydroxyapatite/β-tricalcium phosphate nano-composites using microwave irradiation. Ceram Inter 37:65–71

36. Chen BH, Chen KI, Ho ML, Chen HN, Chen WC, Wang CK (2009) Synthesis of calcium phosphates and porous hydroxyapatite beads prepared by emulsion method. Mater Chem Phys 113:365–371

37. Sopyan I, Pusparini E, Ramesh S, Tan CY, Ching YC, Wong YH, Zainal Abidin NI, Chandran HI, Ramesh S, Bang LT (2017) Influence of sodium on the properties of sol-gel derived hydroxyapatite powder and porous scaffolds. Ceram Int 43:12263–12269

38. Choi AH, Ben-Nissan B (2007) Sol-gel production of bioactive nanocoatings for medical applications. Part II: current research and development. Nanomed 5:51–61

39. Zhou R, Si S, Zhang Q (2012) Water-dispersible hydroxyapatite nanoparticles synthesized in aqueous solution containing grape seed extract. Appl Surf Sci 258:3578–3583

40. Klinkaewnarong J, Swatsitang E, Masingboon C, Seraphin S, Maensiri S (2010) Synthesis and characterization of nanocrystalline HAp powders prepared by using aloe vera plant extracted solution. Curr Appl Phys 10:521–525

41. Gopi D, Kanimozhi K, Bhuvaneshwari N, Indira J, Kavitha L (2014) Novel banana peel pectin mediated green route for the synthesis of hydroxyapatite nanoparticles and their spectral characterization. Spectrochim Acta A 118:589–597

42. Fan TX, Chow SK, Zhang D (2009) Biomorphic mineralization: from biology to materials. Prog Mater Sci 54:542–659

43. Wang YM, Ren XX, Ma XM, Su W, Zhang YP, Sun XS, Li XD (2015) Alginate-intervened hydrothermal synthesis of hydroxyapatite nanocrystals with nanopores. Cryst Growth Des 15:1949–1956

44. Chen JD, Nan KH, Yin SH, Wang YJ, Wu T, Zhang Q (2010) Characterization and biocompatibility of nanohybrid scaffold prepared via in situ crystallization of hydroxyapatite in chitosan matrix. Colloids Surf B 81:640–647

45. Sundrarajan M, Jegatheeswaran S, Selvam S, Sanjeevi N, Balaji M (2015) The ionic liquid assisted green synthesis of hydroxyapatite nanoplates by *Moringa oleifera* flower extract: a biomimetic approach. Mater Des 88:1183–1190

46. Utara S, Klinkaewnarong J (2015) Sonochemical synthesis of nano-hydroxyapatite using natural rubber latex as a templating agent. Ceram Int 41:14860–14867

47. Sasaki T, Kohyama K, Suzuki Y, Okamoto K, Noel TR, Ring SG (2009) Physicochemical characteristics of waxy rice starch influencing the in vitro digestibility of a starch gel. Food Chem 116:137–142

48. Zhang H, Liu Y, Zhou J, Wang J, Sun B (2014) Amylopectin is the anti-fatigue ingredient in glutinous rice. Int J Biol Macromol 63:240–243

49. Lian X, Wang C, Zhang K, Li L (2014) The retrogradation properties of glutinous rice and buckwheat starches as observed with FT-IR, ^{13}C NMR and DSC. Int J Biol Macromol 64:288–293

50. Kadan RS, Champagne ET, Ziegler GM, Richard OA (1997) Amylose and protein contents of rice cultivars are related to texture of rice-based fries. J Food Sci 62:701–703

51. Singh H, Lin JH, Huang WH, Chang YH (2012) Influence of amylopectin structure on rheological and retrogradation properties of waxy rice starches. J Cereal Sci 56:367–373

52. Obeidat M, Shatnawi M, Al-alawi M, Al-Zu'bi E, Al-Dmoor H, Al-Qudah M, El-Qudah J, Otri I (2012) Anti-microbial activity of crude extracts of some plant leaves. Res J Microbiol 7:59–67

53. Kamonwannasit S, Nantapong N, Kumkrai P, Luecha P, Kupittayanant S, Chudapongse N (2013) Antibacterial activity of *Aquilaria crassna* leaf extract against *Staphylococcus epidermis* by disruption of cell wall. Ann Clin Microbiol Antimicrob 12:1–7

54. Guo X, Yan H, Zhao S, Zhang L, Li Y, Liang X (2013) Effect of calcining temperature on particle size of hydroxyapatite synthesized by solid-state reaction at room temperature. Adv Powder Technol 24:1034–1038

55. Sobczak-Kupiec A, Wzorek Z (2012) The influence of calcination parameters on free calcium oxide content in natural hydroxyapatite. Ceram Int 38:641–647

56. Esfahani H, Salahi E, Tayebifard A, Rahimipour MR, Keyanpour-Rad M (2014) Influence of zinc incorporation on microstructure of hydroxyapatite to characterize the effect of pH and calcination temperatures. J Asian Ceram Soc 2:248–252

57. Supachai S, Thananchai D, Sukhontip T (2016) Preparation and characterization of amorphous silica and calcium oxide from agricultural wastes. Orient J Chem 32:1923–1928

58. Shinjiro H, Yuki H, Shan Q, Hirofumi N, Takeshi H (2008) Characterization of calcium carbonate polymorphs with Ca K edge X-ray absorption fine structure spectroscopy. Anal Sci 24:835–837

59. Haberko K, Bućko MM, Brzezińska-Miecznik J, Haberko M, Mozgawa W, Panz T, Pyda A, Zarębski J (2006) Natural hydroxyapatite-its behavior during heat treatment. J Eur Ceram Soc 26:537–542

60. Akram M, Ahmed R, Shakir I, Ibrahim WAW, Hussain R (2014) Extracting hydroxyapatite and its precursors from natural resources. J Mater Sci 49:1461–1475

61. de Groot K (1983) In: de Groot K (ed) Bioceramic of calcium phosphate. CRC Press, Florida

62. Türk S, Altinsoy İ, ÇelebiEfe G, Ipek M, Özacar M, Bindal C (2017) Microwave-assisted biomimetic synthesis of hydroxyapatite using different sources of calcium. Mater Sci Eng C 76:528–535

63. Bucur AI, Bucur RA, Szabadai Z, Mosoarca C, Linul PA (2017) Influence of small concentration addition of tartaric acid on the 220 °C hydrothermal synthesis of hydroxyapatite. Mater Charact 132:76–82

64. Ashok M, Sundaram NM, Kalkura SN (2003) Crystallization of hydroxyapatite at physiological temperature. Mater Lett 57:2066–2070

65. Mishra VK, Bhattacharjee BN, Parkash O, Kumar D, Rai SB (2014) Mg-doped hydroxyapatite nanoplates for biomedical applications: a surfactant assisted microwave synthesis and spectroscopic investigations. J Alloy Compd 614:283–288

66. Liu J, Ye X, Wang H, Zhu M, Wang B, Yan H (2003) The influence of pH and temperature on the morphology of hydroxyapatite synthesized by hydrothermal method. Ceram Int 29:629–633

67. Lu X, Fan Y, Gu D, Cui N (2007) Preparation and characterization of natural hydroxyapatite from animal tissues. Key Eng Mater 342–344:213–216

68. Agnieszka S, Zygmunt K, Zbigniew W (2009) Preparation of hydroxyapatite from animal bones. Acta Bio Eng Biomech 11:23–28

69. Nathanael AJ, Mangalaraj D, Chen PC, Nataraj D (2010) Improved mechanical property of hydrothermally synthesized hydroxyapatite nanorods reinforced with polyethylene. Int J Mod Phys B 24:215–223

70. Jin T, He YP (2011) Antibacterial activities of magnesium oxide (MgO) nanoparticles against foodborne pathogens. J Nanopart Res 13:6877–6885

71. Tang ZX, Lv BF (2014) MgO nanoparticles as anti-bacterial agent: preparation and activity. Braz J Chem Eng 31:591–601

72. Valle Jr. DL, Andrade JI, Puzon JJM, Cabrera EC, Rivera WL (2015) Antibacterial activities of ethanol extracts of Philippine medicinal plants against multidrug-resistant bacteria. Asian Pac J Trop Biomed 5:532–540

73. Hsouna AB, Trigui M, Mansour RB, Jarraya RM, Damak M, Jaoua S (2011) Chemical composition, cytotoxicity effect and antimicrobial activity of *Ceratonia siliqua* essential oil with preservative effects against *Listeria* inoculated in minced beef meat. Int J Food Microbiol 148:66–72

74. Gokcekaya O, Ueda K, Ogasawara K, Kanetaka H, Narushima T (2017) In vitro evaluation of Ag-containing calcium phosphates: effectiveness of Ag-incorporated β-tricalcium phosphate. Mater Sci Eng C 75:926–933

75. Jamil M, Abida F, Hatim Z, Elassfouri M, Gourri E (2015) Effects of ions traces on the dissolution of bioceramics composed of hydroxyapatite and β-tricalcium phosphate. Med J Chem 4:51–58

76. Li X, Ito A, Wang X, LeGeros RZ (2009) Solubility of Mg-containing β-tricalcium phosphate at 25 °C. Acta Biomater 5:508–517

77. Xie Y, Yang L (2016) Calcium and magnesium ions are membrane-active against stationary-phase *Staphylococcus aureus* with high specificity. Sci Rep 6:20628. https://doi.org/10.1038/srep20628

78. Brown L, Wolf JM, Prados-Rosales R, Casadevall A (2015) Through the wall: extracellular vesicles in Gram-positive bacteria, mycobacteria and fungi. Nat Rev Microbiol 13:620–630

79. Sikkema J, De Bont JA, Poolman B (1995) Mechanisms of membrane toxicity of hydrocarbons. Microbiol Rev 59:201–222